An Overview of Helium Ion Microscopy

Materials Characterization Report

MSE 505 Assignment (I)

Edward Deleu

edeleu@princeton.edu

MSE 505: Characterization of Materials

Professor Nan Yao

Spring 2025

Due: April 25, 2025

Contents

1 Helium Ion Microscopy for Nanoscale Characterization 2

2 Background & History 4

2.1 Historical Development 4

2.2 Modern Advances 5

3 Instrumentation of Helium Ion Microscopy 6

3.1 Gas Field Ion Source (GFIS) 6

3.2 Ion Optics 8

4 Sample Interaction and Imaging Principles 10

4.1 Secondary Electrons 12

4.2 Backscattered Ions 15

4.3 Ionoluminescence 17

5 Analytic Capabilities of HIM 17

5.1 Secondary Ion Mass Spectrometry 18

5.2 Backscattering Spectrometry 19

6 Comparison to Scanning Electron Microscopy (SEM) 21

7 Applications of HIM 24

7.1 High-Resolution Imaging of Biological Samples 24

7.2 Crystallographic Orientation Mapping 26

7.3 Subsurface Imaging 27

7.4 Ionoluminescence Imaging 28

7.5 SIMS Imaging 29

8 Summary and Future Perspectives 31

1 Helium Ion Microscopy for Nanoscale Characterization

Helium Ion Microscopy (HIM) is an advanced microscopy technique utilizing a focused beam of helium ions to generate ultra-high-resolution images of samples. The ion beam is raster scanned over a sample's surface and an image is formed through the detection of emitted secondary electrons (SE). A modern helium ion microscope, the Zeiss ORION NanoFab, is pictured in Fig. 1. This technique is versatile, allowing for significant capabilities beyond the ultra-high-resolution analysis and imaging of samples. It is especially well-suited for biological samples, with widespread applications across materials science and nanofabrication.

In principle, HIM is very similar to scanning electron microscopy (SEM), replacing the electron beam with a beam of ions. The ions are several orders of magnitude higher in mass than electrons: an electron has a mass of approximately $m_e = 9.109{\times}10^{-31}$ kg, yet a helium ion has a mass of $m_{He^+} = 6.646 \times 10^{-27}$ kg, a difference of nearly 7300×. This results in remarkably smaller wavelengths for the helium atoms and is the primary factor allowing for extremely high resolution surface imaging. By decreasing the wavelength of the particles, they may inherently be focused to a smaller spot size.



Figure 1: Photograph of the Zeiss ORION NanoFab microscope, reproduced from Zeiss [1].

A particle's energy directly corresponds to its acceleration voltage: for example, a helium ion accelerated at a voltage of 20kV will have 20keV of energy, assuming that $E = qV$ and the particle is singly ionized. In general, de Broglie wavelength may be given by $\lambda = h/p$. For electrons, relativistic corrections should be made since they travel at high velocities, especially at acceleration voltages above 80kV. Their wavelength may be given by the expression

$$\lambda_e = \frac{h}{p} = \frac{h}{\sqrt{(\frac{eV}{c})^2 + 2m_e eV}} \tag{1}$$

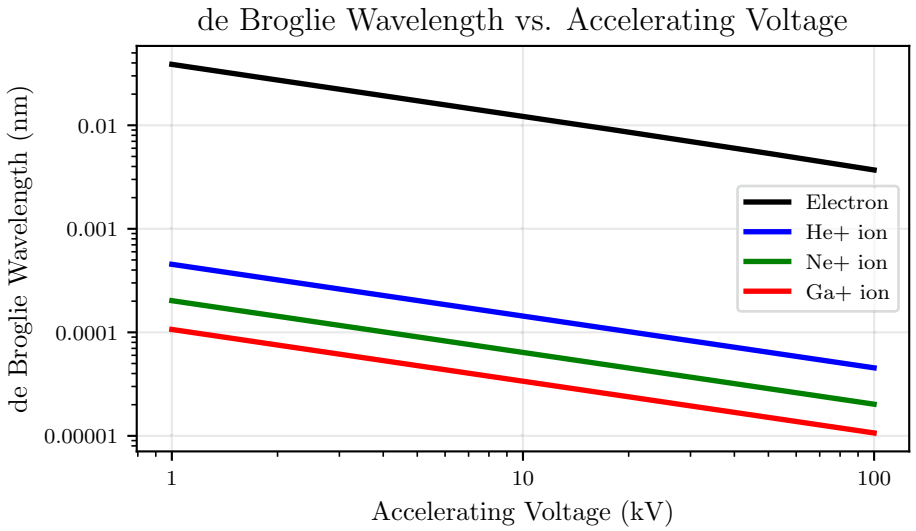


Figure 2: Comparison of the de Broglie wavelength of electrons and various ions as a function of their acceleration voltage.

where λ_e is the de Broglie wavelength of the electron, h is Planck's constant, e is the fundamental unit of charge, V is the acceleration voltage, m_e is the mass of an electron, and c is the speed of light. For helium ions, since their mass is approximately 3 orders of magnitude greater than electrons, relativistic corrections are not necessary. Thus, their wavelength may be given by the expression

$$\lambda = \frac{h}{\sqrt{2meV}} \tag{2}$$

where m is the mass of the ion. With these expressions, it is possible to plot the de Broglie wavelength of electrons and various ions vs. acceleration voltage, as displayed in Fig. 2. This displays how helium ions have a wavelength over an order of magnitude less than electrons accelerated at the same voltage. At 30kV, a He^+ ion will have a wavelength of 0.083pm, while an electron will have a wavelength of 7.0pm, an over 84× difference. As a consequence, imaging with ions rather than electrons will have a more favorable wavelength, theoretically allowing for better resolution and capturing sub-atomic details. The other ions depicted, Ne^+ and Ga^+, have even lower wavelengths and are frequently used in HIM systems for sputtering and nanofabrication capabilities [1].

2 Background & History

The development of the first ion beam microscopes were inspired by the principles and developments of scanning electron microscopy. In general, it is desirable for the illumination source of a microscope to emit the highest amount of radiation possible into the smallest area, all while maintaining a finely focused parallel beam [2]. It is also desirable for the illumination source to have a minimal energy spread so that the microscope comes into focus at a single distance. Scanning electron microscopes utilize a cold field emission gun as a source: there is a filament of tungsten wire with a very sharp tip in an ultra-high vacuum. When a high enough negative voltage is applied at this tip, electrons will begin to flow to ground [2].

2.1 Historical Development

The field ion microscope (FIM) was developed by Erwin Müller at Penn State in the early 1950s. This microscope consisted of a sealed chamber filled with helium gas. At one end was a cryogenically cooled metal needle with a tip sharpened to a radius of about 100nm. The other end had a fluorescent viewing screen. By applying several kV to the tip, a strong field near 4V/Å is produced. An approximately empty spherical region is formed at this tip: any atoms and defects are essentially evaporated away. Directly beneath the individual atoms of the tip, there are disk-like regions of extremely high field strength where quantum-mechanical tunneling of electrons may occur between the atoms of helium gas and the metallic atoms at the tip of the needle. When gas atoms pass through the "ionization-disk," the atoms become positively charged and are accelerated toward the fluorescent screen: this is the helium ion beam [2]. This is the basis for the first ion microscope: an image displaying the atomic arrangement of the tip of the needle is directly produced on the fluorescent screen. This microscope allowed for the visualization of individual atoms for the first time in history [3].

This powerful development of an ion beam would later allow for the creation of a dedicated ion microscope to observe arbitrary samples. University of Chicago Professor Ricardo Levi-Setii

developed a scanning transmission ion microscope, utilizing an H^+ beam at a voltage of 65kV. He combined the ideas of the field emission gun used in electron microscopy with the earlier field ion microscope using a single-crystalline tungsten needle as the tip [4]. A partnership between JEOL and Micrion was later formed to commercially adopt the gas field ion source (GFIS) for the semiconductor industry.

2.2 Modern Advances

The first true commercial helium ion microscope was developed by the Atomic Level Imaging Systems (ALIS) corporation in 2006, named ORION [3]. ALIS was acquired by Carl Zeiss in 2007, leading subsequent development of the ORION microscopes. Zeiss's second-generation helium ion microscope was first delivered in 2012, the ORION NanoFab. This microscope not only supports helium atoms, but it is capable of using beams of neon or gallium and is primarily intended for nanofabrication with a sub-10nm precision [1]. A dedicated source exists for the Ga^+ beam, but the same GFIS may be utilized with either neon or helium gas to produce these ion beams. These other ion types interact differently with samples and are mostly used for nanofabrication purposes like ion milling, implantation, or sputtering, and are thus outside the scope of this report [2]. Zeiss markets the ORION NanoFab to have a 0.5nm resolution at 30kV with the helium ion beam.

To date, the ORION series of ion microscopes have been the only dedicated ion microscopes commercially available. Still, there exist other "dual-beam" scanning microscopes with both electron and ion beams, although the ion beams are most commonly Ga^+ and are intended for nanofabrication or sample preparation [2]. While Zeiss's ORION NanoFab system is the most advanced helium ion microscope system, Zeiss seems to have since discontinued its entire ORION lineup and all dedicated Helium Ion Microscope products. Its ORION and ORION Plus systems reached official end of life in October of 2023, and little information about the helium ion microscopes remains on their website.

3 Instrumentation of Helium Ion Microscopy

A helium ion microscope system comprises of several key components: a helium ion source that produces an ion beam; a column equipped with optics to minimize aberrations and focus the beam at the sample's surface; and finally, detectors that capture secondary electrons and other signals emitted from the sample. These components enable the generation of high-resolution images with exceptional surface detail. Fig. 3 displays a simplified schematic diagram of a helium ion microscope, highlighting its most crucial components.

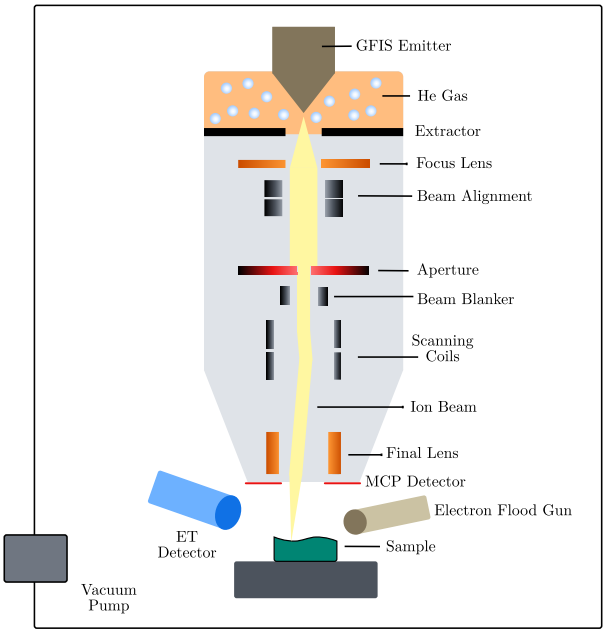


Figure 3: Schematic diagram of a helium ion microscope.

3.1 Gas Field Ion Source (GFIS)

The gas field ion source (GFIS) introduced in Sec. 2.1 is the key component allowing for successful ion microscopy, represented schematically in Fig. 4a. A positively biased needle with an atomically sharp tip acts as the electrode from which the ion beam originates. Either helium or neon gas may be used with the GFIS, although the technique is called helium ion microscopy regardless. The ion source is cryogenically cooled to temperatures between 75-80K from an integrated liquid nitrogen dewar [5]. A high positive voltage is applied to the tip, on the order of 10's of kV. The neutral gas atoms are absorbed onto the tip and ionized through a field ionization process. The atoms are polarized due to the very high electric field here, and electrons may tunnel from the gas atoms to the metal tip. This produces the positively charged ion beam of He^+ or Ne^+ atoms [6]. It is crucial to have an extremely high vacuum in the GFIS: in the absence of imaging gases, the base pressure

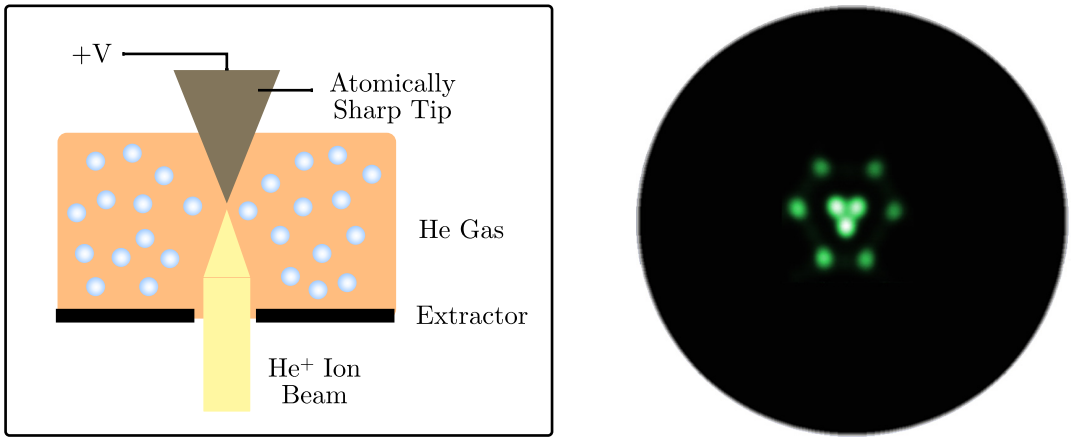


Figure 4: (a) Schematic diagram of the ionization of helium at the tip of the GFIS. (b) The appearance of a typical trimer emission pattern, reproduced from Zeiss [1].

should be $< 4 \times 10^{-10}$ Torr [5].

The needle is a single-crystalline wire approximately 5mm long with a diameter of 0.25mm, terminating in a sharp 30° cone. The material of the needle and shaping process are proprietary [2], although Tungsten was initially chosen due to its mechanical strength and ability to encounter high electric fields. The tip is shaped and faceted from a hemispherical form in a modernized version of the original field ion microscope with liquid nitrogen cooling. The shape is optimized such that its atoms are stripped away until the tip contains just three atoms left in a triangular trimer arrangement. This arrangement is stable and optimizes the He^+ ion current, also maximizing vertical emission forming a collimated ion beam. Each of the three atoms effectively creates its own ion beam: using apertures and beam optics, only one of these beams is selected to probe the sample with [6]. The emission pattern of the tip is seen in Fig. 4b, produced with the aforementioned field ion microscope setup. This image displays how the three trimer atoms have the highest emission intensity. The ORION microscope includes automated procedures which may generate a new trimer pattern at the tip of the electrode by increasing the bias voltage to sufficiently high values [2].

Two important parameters of the GFIS are the gas pressure and tip temperature. The gas pressure is linearly proportional to the beam current, with a maximum emission current of 50-100pA [2]. A typical imaging gas flux is around $Q = 4 \times 10^{-4}$ Torr liter/s. High gas purity is ensured through an

activation purification process as well as passing the gas through a cryogenically cooled delivery system [5]. If the tip temperature is too low, the process by which gas atoms are absorbed will occur too slowly. If the tip temperature is too high, the atoms will remain stuck to the tip for too long. It is best practice to limit the beam current from a single atom to around 10pA: the emission is best left around 1pA or lower during typical operation [2].

The GFIS source has favorable properties for microscopy applications. The source size of the ion beam is effectively just a single-atom in diameter, and for helium is claimed to be around 3Å [3, 6]. The spread in energy of the ion beam is less than 1eV, minimizing the effects of any chromatic aberrations due to a spread in ion energy [3]. The beam has an image side semi-convergence angle on the order of 100μrad, one to two orders of magnitude lower than comparable values from electron sources [2]. Chromatic and spherical aberrations will impact the probe quality much less than with SEMs, since spherical aberrations vary with α^3 and chromatic aberrations with α. Thus, the HIM does not require any aberration correction system to achieve its sub-nanometer resolution [2]. The brightness of the GFIS beam is on the order of 10^9 A $\cdot$ (cm^2 sr)$^{-1}$, comparable to an electron field emission gun at the same acceleration voltage [2, 6].

The optimal bias voltage for a GFIS depends on the tip geometry. Sharper tips will more effectively concentrate the electric field, requiring lower voltages, while more rounded tips will require higher voltages to achieve the same field strength. For helium ions, the best imaging voltage is achieved for a field strength of 4.4 V/Å at the tip [2]. It is crucial not to exceed the optimal field strength, as too high of a bias voltage will destroy the tip, stripping away its atoms. The extractor serves as the reference-point, with a small positive bias near zero to fine-tune the ion extraction. The tip is typically biased between 25 to 35kV: lower voltages are not necessary, and this is typically not a parameter that requires tuning during HIM operation [2].

3.2 Ion Optics

A series of ion optics allows for the precise focusing, alignment, and scanning of the ion beam, displayed in Fig. 3. The optics include electrostatic lenses, scanners, and deflectors. These optics

may be adjusted and calibrated to perfectly focus the beam and raster scan it across a sample to collect information point-by-point. Various sized apertures may be used in order to control the size of the beam. Since helium ions have such a small wavelength, diffraction effects are limited in helium ion microscopy [2, 3]. Extremely small apertures may effectively be used to minimize probe size and greatly enhance depth of field, although decreasing beam current. In many cases, the depth of field can be comparable to the horizontal field of view for an image. One highlight of imaging with HIM is the long depth of field that may be achieved, as a result of the small wavelength and convergence angle. The original introduction to helium ion microscopes proposed an optimally achievable probe size of 0.25nm [3]. With a detailed breakdown, the optimal probe size that may be achieved at 30kV with 0.5pA is 0.35nm with an image-side beam semi-convergence angle of α = 0.35mrad. Practically speaking, probe sizes between 0.35-0.5nm are realistic and depend on exact operating conditions. The minimum feature size that may be resolved is around 3nm with helium ions. The limiting factors of the probe size are the source brightness and chromatic aberrations, followed by diffraction and spherical aberrations. Still, these factors and their contributions depend on the exact system setup and adjustments [5].

The path of the ion beam, starting as it passes through the GFIS extractor, will now briefly be discussed. For a given emission site of the trimer, a specific calibration and alignment of the ion column is necessary. The first lens, often called the condenser or focus lens, brings the beam to a cross-over inside the column. In an ideal scenario, the beam should travel directly along the axis of the lenses. Alignment may be accomplished mechanically with tilt and shift of the lens, electronically with deflectors, or a combination of the methods [5]. After the beam passes through the first lens, a beam alignment step is performed through a double deflection system to correctly align the beam for the axis of the final lens. An operator may optimize beam brightness and minimize beam motion (“wobble”) by adjusting these deflectors which are often quadrupoles [7]. Subsequently, the aligned beam passes through the beam limiting aperture: this effectively controls the probe size and beam current. The aperture should have a maximal distance from the condenser lens to maximize the range of adjustment for the probe current. For a helium beam, the

optimum aperture material is a thin film of gold: this reduces scattering but has a short lifetime due to sputtering by constant exposure to the ion beam. Then, the beam passes through the beam blanker: this electrostatic device allows for the beam to be blanked. Effectively, this determines whether the ion beam passes through to the sample or is here interrupted [5].

Up to this point, a narrowly focused and aligned beam profile has been produced. However, this beam must scan across the sample: a dual-deflection system allows for this functionality, electrostatically deflecting the beam, most commonly with octopoles. The deflectors, often called scanning coils, are set up so that the beam still passes through the center of the final lens where aberrations are minimized. Placement of this deflection system before the final lens allows for a smaller working distance between the sample and final lens [5]. The first deflector of this deflection system is also responsible for astigmatism correction, correcting for an asymmetric beam profile. The final lens, the objective lens, images the beam onto the sample. Of course, this is a simplified view of the optics, but these are the main components required to precisely focus and control the ion beam.

In total the time of flight for a 30keV helium ion traveling through a distance of 10cm is 83ns [5]. Thus, a non-negligible amount of time traveling through the ion column must be considered in the scanning of the ion beam and collection of signals.

4 Sample Interaction and Imaging Principles

HIM operates by scanning a focused helium ion beam across a sample surface. Interactions between the helium ions and the sample produce several types of signals, depicted in Fig. 5. These signals produced by the ion-sample interactions are critical in interpreting detailed sample information at the nanometer scale. One of the most important signals are the secondary electrons which may directly be collected to form an image, as in scanning electron microscopy.

HIM allows for the imaging and analysis of both conductive and non-conductive samples. Conductive samples must be grounded so the surface does not build up positive charge from the

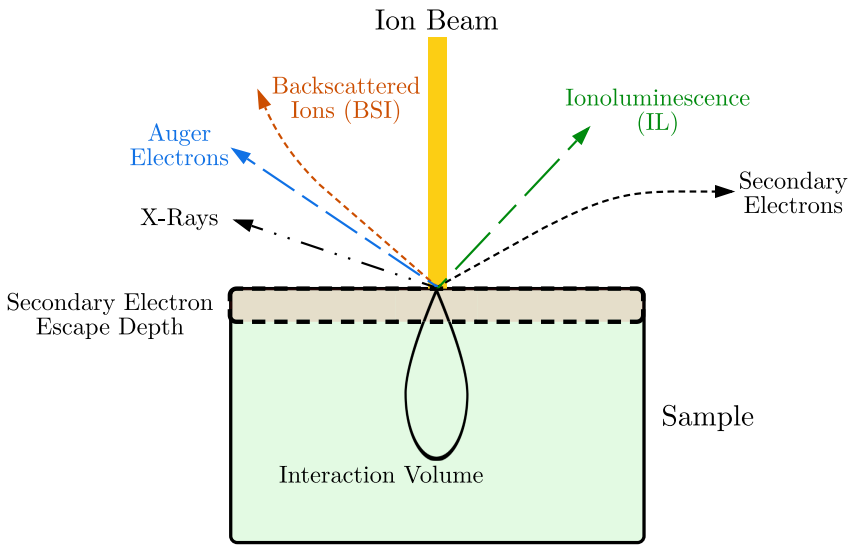


Figure 5: Diagram of the various signals emitted from a sample under irradiation from an ion beam.

ion beam. For non-conductive or insulating samples, the surface *will* become positively charged from the positive helium ions. This will negatively impact the emission of secondary electrons required for imaging. An electron flood gun is typically installed in the HIM chamber: this directs a low energy electron beam onto the sample surface to prevent any charge from building up, and this is a highly effective technique [6]. Thus, sputter coating non-conductive samples or utilizing specialized equipment is not required as may be the case with SEMs. Sputter yield is defined as the number of sample atoms removed per incident ion. For a helium ion beam, sputter yield is quite low for most materials and causes negligible sample damage at typical acceleration voltages [2]. For example, for helium ions and a silicon substrate, the sputter yield is below 0.1 atoms/ion [2]. In comparison, neon ions have a lower implant depth and higher sputter yield due to their higher mass.

A sample's interaction volume is the volume within which the ion beam penetrates and scatters. Penetration depth may be considered as the average maximum depth which the particles may travel for a given sample. Once helium ions dissipate their energy traveling within a sample, they may become implanted. At sufficiently high ion doses, it is possible for small gas bubbles to form under the surface of a specimen [6]. Fig. 6 indicates this phenomena for graphene flakes on a SiO_2

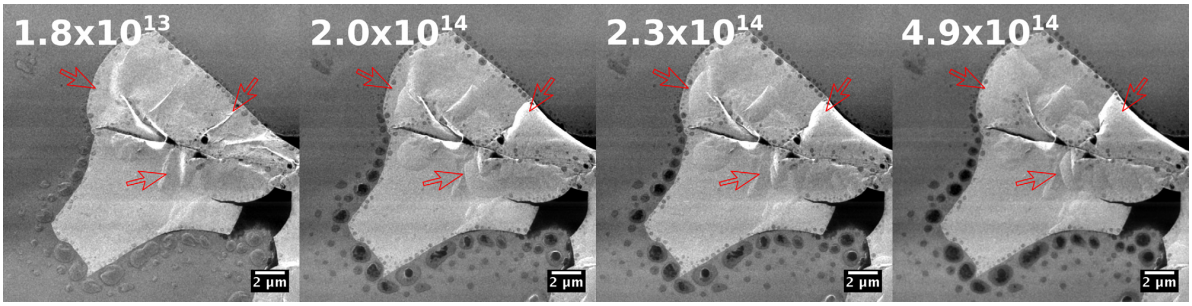


Figure 6: SE image series of the formation of bubble defects (indicated by red arrows) on a graphene flake for increasing helium ion doses in ions $\cdot$ cm^{-2} indicated in white text on each panel. Adapted from [8].

substrate. As the ion exposure increases, the subsurface bubble in the top left area of the graphene flake continuously expands in size. In contrast, the bottom-most bubble increases in size in the first two panels, subsequently decreasing in size as the helium escapes through defects in the flake. According to estimates, the gas pressure of these bubbles is likely around 10 mbar [8]. It is notable that these flakes may be imaged with great contrast despite their ultra-thin nature.

To approximate the penetration depth by a beam of charged particles, the Kanaya-Okayama expression may be used: it relies only on the particle energy and the sample density. For electrons, it may be given as

$$R_{KO} = \frac{0.0276A \cdot E^{1.67}}{\rho \cdot Z^{0.89}} \tag{3}$$

where R_{KO} is the penetration distance in µm, E is the particle energy, A is the atomic weight of the sample, Z is the atomic number, and ρ is the density of the sample [9]. While the constants vary for various ion beams compared to electrons, the functional form is similar. For ions, the energy factor changes to $E^{0.72}$ [2]. For a given material and acceleration voltage, electrons will penetrate between 1-2 orders of magnitude deeper than ions.

4.1 Secondary Electrons

Secondary electrons (SEs) are defined as electrons emitted from a sample that have been ionized as a result of an incident high-energy particle [2]. If the electrons are sufficiently close to the sample surface and have enough energy, they may escape the bulk of the sample [6]. Typically, secondary

electrons are only considered to be those emitted with energies less than 50eV. In metals, the mean escape depth of SEs is typically around 1-5nm [10]. These electrons lose energy by interacting with conduction electrons and impurities [11]. In insulators, mean escape depths are on the order of 10-20nm [10]. These electrons encounter much less electron-electron scattering as a result of large band gaps and relatively few conduction band electrons [11]. In both scenarios, the maximum escape depth may be as much as 5× the mean.

With SEMs, there is often the distinction between SE1 and SE2, where SE1 are produced by primary beam interactions and SE2 are emitted away from the initial probe area as a result of electrons (or ions) that are backscattered in the sample and subsequently knock away electrons. While SE1s contain surface information, SE2s degrade image contrast and are undesirable, even dominating entire SE yield in many situations [2]: fortunately, SE2s are not as dominant in HIM as they are with SEMs. Another benefit of helium ions is an increased SE yield compared with electron beams: the yield is typically 3-5x higher and is typically 2-8 electrons per incident ion at typical HIM energies with metal samples [2, 12, 13]. Whereas SE production in SEMs is roughly constant, SE production with ion beams greatly increases with acceleration voltage [2]. Thus, for all practical purposes, a HIM should be operated at its rated voltage at all times, somewhere near 30kV. Reducing the voltage only decreases signal yield and there are not major benefits to image quality besides a somewhat reduced beam penetration [2].

Fig. 7 depicts the sample interaction of a bulk silicon sample with electron and helium ion beams. The electron beam at 1keV has limited penetration-depth: however, the electrons spread out significantly, including near the surface of the sample. In SEMs, minimizing the beam voltage is often desirable for the best imaging resolution since the interaction volume is minimized. Still, with a 1kV beam the interaction area within the secondary electron escape depth is significantly larger than the probe-size. Thus, secondary electrons **will** be generated outside the region that the beam is probing. This behavior is undesirable, decreasing the quality of the resulting image since features get blurred. Inherently, SE imaging from an electron beam carries significant information from deep within a sample as a result of SE2s from electron backscattering. In contrast, the 30keV

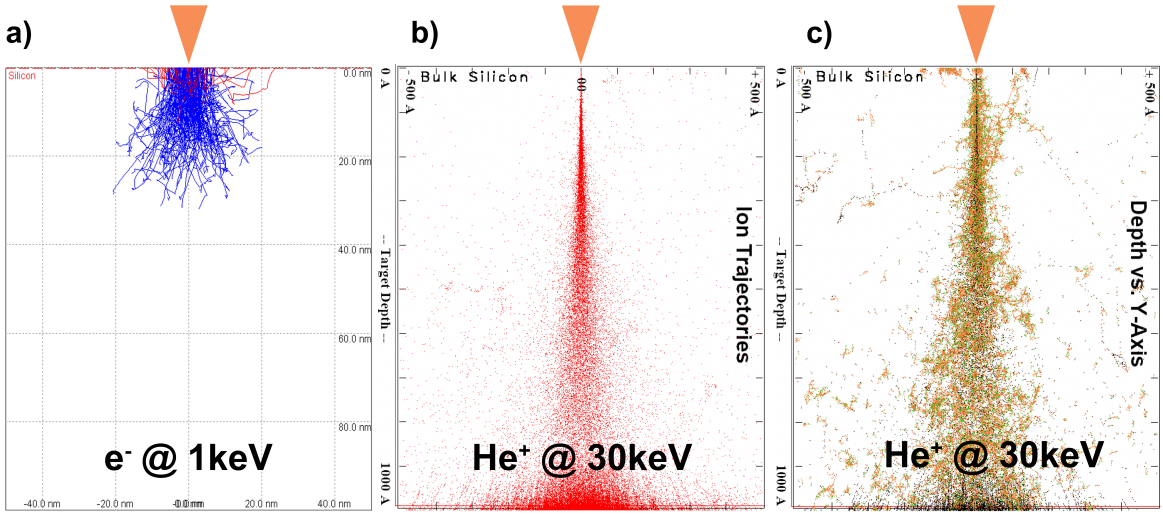


Figure 7: Monte-Carlo simulations of electron and helium ion trajectories as a function of depth for a bulk-silicon substrate. The FOV is $100nm \times 100nm$ for each simulation. (a) CASINO simulations of 300 electron trajectories at 1keV. (b) Transport of Ions in Matter (TRIM) ion trajectories with no recoil for 3000 simulated interactions. (c) Ion trajectories with recoil and sample interactions visualized for 750 simulated incident ions.

helium ion beam does not spread out significantly within the secondary electron escape depth. The beam penetrates deeply into the sample before significantly diverging. Thus, the secondary electrons do not convey information from an area much larger than the probe size itself. This is extremely desirable, allowing for better edge clarity and imaging quality overall. This is a significant benefit of HIMs compared to SEMs.

To detect the secondary electron signal from a sample, an Everhart-Thorney (ET) detector is used, just as with SEMs [6]. This detector has a fine mesh grid that is positively biased around 500V in order to attract secondary electrons emitted from the sample. As the ion beam scans across the sample surface, the ET detector will measure relative counts of SEs. Then, the electron intensities may be mapped to the corresponding positions on the sample to form a grayscale image. Brighter regions have higher SE yields, while dimmer regions have less SE yield. This forms the basis for imaging with a helium ion microscope.

Several distinct mechanisms are responsible for the contrast in secondary electron imaging. First, and most importantly, is the topography of the sample and the angle at which the beam is incident upon a surface. This topographical contrast and imaging mode is most intuitive: the light

source is effectively the position of the ET detector and the observer is effectively positioned above the sample looking straight down the ion beam [2]. This yields images that look intuitive and straightforward to understand. The SE yield and hence image intensity is proportional to the angle of beam incidence with the sample surface: the closer the angle is to 90°, the higher the yield will be. The SE yield may be roughly approximated by the secant law,

$$\delta(\theta) = \delta_o \sec(\theta) \tag{4}$$

where $\delta(\theta)$ is the SE yield as a function of the specimen tilt θ and δ_o is a yield constant [8]. Another contrast mechanism is composition: secondary electron yield in HIM is sensitive to the material composition and atomic number Z, much more so than with SEMs [5, 13, 14]. This is a complex and often non-monotonic contrast mechanism that is experimentally observed. Any electric potentials and voltage differences on the sample will also provide contrast [3]. HIM allows for more sensitive surface imaging as a result of the decreased interaction volume and increased SE yield.

Another notable mechanism of contrast results from ion channeling in crystalline samples. If the ion beam is incident in a low miller-index direction, the ion beam may channel through the lattice without experiencing collisions [13]. This channeling thereby decreases SE yields. Different grains in a polycrystalline sample will form channeling contrast in a SE image, similar to electron backscatter techniques in SEMs for mapping grain orientations.

4.2 Backscattered Ions

A portion of the incident ion beam is backscattered off the sample– that is, it is deflected away. These are known as Rutherford Backscattered Ions (RBI) and may be imaged in a technique sometimes referred to as Rutherford Backscatter (RBS) imaging [14]. These scattered ions have similar energy to the incident ion beam. While an ET detector with no bias voltage may theoretically be used to collect RBI information, this is not ideal. Optimal placement for a backscattered ion detector is

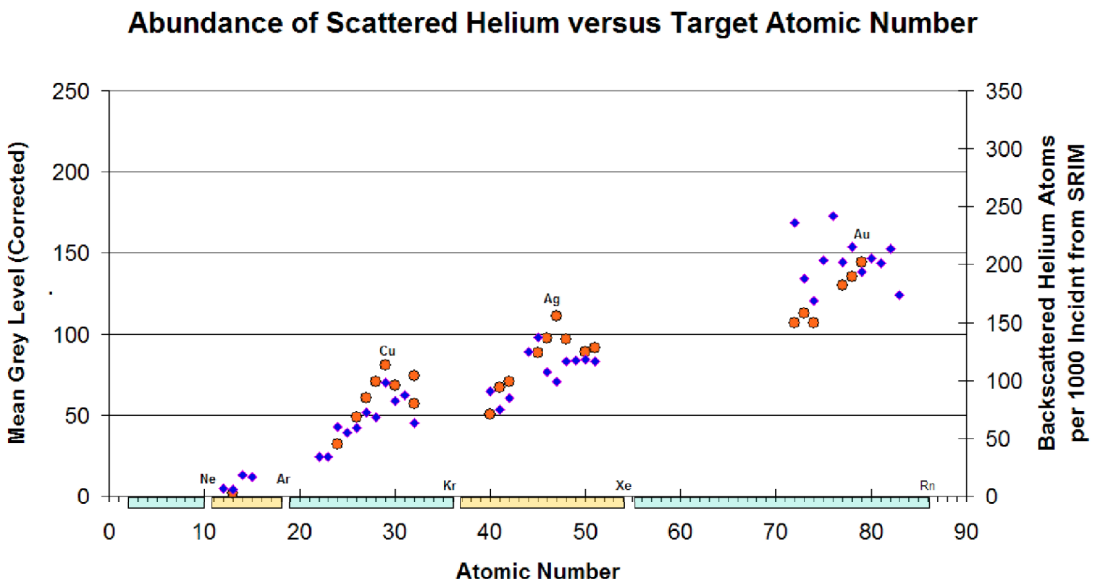


Figure 8: Yield of backscattered helium ions vs. atomic number Z. The orange circles and left-axis represent experimental brightness values, while the violet diamonds and right axis represent backscatter yields out for 1000 incident ions using Stopping and Range of Ions in Matter (SRIM) simulations. Reproduced from [3].

directly above the sample, between the final lens of the ion column and the sample. The detector may be negatively biased as to repel SEs. Two types of RBI detectors are the micro-channel plate detector (MCP) and the silicon drift detector (SiDD) [2]. Backscattered ions primarily provide information about material contrast, while topographic contrast is significantly reduced compared to imaging with SEs as a result of the high ion energy [14]. Differences in backscatter yield are closely related to atomic number Z, and this "Z-contrast" is the primary contrast mechanism in ion backscatter imaging. The exact relationship is oscillatory (especially near atoms with compute valence shells), but in general, RBI images are brighter in regions of high atomic number [2]. This relationship is depicted in Fig. 8 for backscattered helium ions in various materials. Elements with atomic number less than 20 have almost negligible backscatter yields according to the simulations, while heavier elements like Au and Ag have significant backscatter yield. RBI is a particularly interesting imaging mechanism since images may be formed of structures covered by thin films of low atomic number materials. Ion channeling also causes decreased backscatter yield for certain crystallographic orientations aligned with the beam, just as with SEs.

4.3 Ionoluminescence

Ionoluminescence (IL) is the emission of photons (light) due to electronic transitions within a sample, as a result of the incident ion beam. Electrons may be excited to higher energy states, subsequently relaxing and transitioning to lower energy levels through photon emission. Photon emission from the ion species of the beam is possible, but it is mostly of interest to study emission from the sample itself. Studies on ionoluminescence with HIM are quite limited since the amount of light emission is very low, and emission from the ion beam further complicates analysis [6]. IL may be split up into two main categories based on the source of light emission: (1) linked to impurities in a sample (extrinsic IL) and (2) linked to recombination of free electrons (intrinsic IL). The presence of certain ions in a sample may reduce the likelihood for emission while others may promote photon emission. As a sample is continuously exposed to an ion beam, however, optical properties and luminescence may change as defects are formed. Enhanced emission may result, such as in alkali halides, or reduced emission may result, as in semiconductors and quantum dots [8]. IL allows for the tracking of defects as a sample is exposed to an ion beam and its light emission changes. Imaging using IL is an interesting technique, although it has seen quite limited applications as a result of the numerous associated difficulties.

5 Analytic Capabilities of HIM

Besides the aforementioned imaging techniques, the signals produced by a sample exposed to an ion beam may be used in various analytic techniques. Besides secondary ion mass spectrometry (SIMS), however, the analytic techniques have many challenges and are not very well suited for use with HIM. For example, consider Auger electron spectroscopy. An incident ion beam may lead to the emission of Auger electrons, from either the sample atoms or incident ions themselves. This occurs when the ion beam ejects inner-shell electrons to create holes which are subsequently filled: the released electrons have properties characteristic to the element they originate from. While ion-induced Auger spectroscopy is a valid technique, there currently exist no studies on

ion-induced Auger electron spectroscopy using HIMs [6, 13]. This may be explained by a simple fact: Auger emission from helium ions tends to dominate at low energies in the range of 100s of eV, which is far below the typical ion beam energy [5, 6].

5.1 Secondary Ion Mass Spectrometry

By far the most popular analytic capability of HIM besides secondary-electron imaging is secondary ion mass spectrometry (SIMS). This technique will only be covered briefly, although many comprehensive reviews of the technique exist [6, 13]. As incident helium ions penetrate into a sample, they will progressively lose their energy as they collide with target atoms. The collisions may result in the sputtering of target atoms, recoils, or implantation of the beam ions. During the sputtering process, it is possible for target atoms to spontaneously ionize, resulting in secondary ions. Additionally, entire clusters of atoms may ionize, maintaining some of the original sample structure [2]. These ions may be collected by an electric field and injected into a mass spectrometer to perform SIMS [13]. Different ions may here be filtered according to their mass-to-charge ratio and finally detected [6]. This technique has extraordinary sensitivity to detect both major and trace elements, with very high mass resolution and the ability to differentiate between different isotopes. The secondary ion signal for an element M can be given as

$$I_M = I_p \cdot Y \cdot C_M \cdot \beta_M \cdot \tau \tag{5}$$

where I_p is the current of the incident ion beam, Y is the sputtering yield, C_M is the concentration of the given element M, β_M is the probability of ionization, and τ is the detection efficiency of the mass spectrometer. While this technique may be performed with helium ions, it is much more successful with neon ions since they have an order of magnitude higher sputtering yield [13]. In order to maximize the secondary ion signal and β_M resulting from nonreactive He^+ or Ne^+ ions, the chamber may be flooded with O_2 gas to optimize the emission of positive secondary ions or Cs gas for negative secondary ions [13]. A schematic diagram of a dedicated SIMS system designed

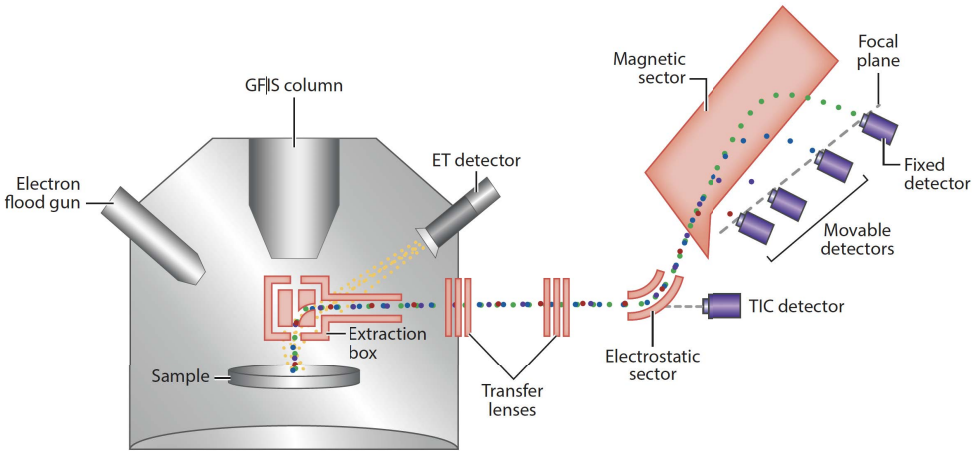


Figure 9: Simplified schematic diagram of the magnetic sector SIMS system attached to a helium ion microscope. Reproduced from [13].

for the HIM is depicted in Fig. 9.

SIMS with the helium ion microscope has be used for two main types of analysis: obtaining mass spectra and imaging. When determining mass spectra, the SIMS technique has incredible sensitivity and resolution to determine the surface composition of a sample. SIMS imaging works similarly to the more typical SE imaging: the ion beam is scanned across the sample and maps are produced correlating specific pixels to the presence of different ions. These may be color-coded and overlaid above a typical SE image to produce a beautiful compositional map of a sample, or alternatively fused through more complicated image processing algorithms [6]. In practice, this method allows for sub-10nm imaging, a significant improvement compared to conventional SIMS imaging techniques [13].

5.2 Backscattering Spectrometry

Backscattered He^+ ions result when the incident ions elastically scatter off the sample. Rutherford backscattering spectrometry is typically performed with MeV range particles, allowing for the identification of sample particles through the beams backscatter energy. The technique is difficult to conduct with low ion energies in HIM <35keV [13]. The technique heavily relies on comparison to simulations which is complicated by screening effects and multiple scattering events. Detectors

must also be able to detect neutral particles as well as charged ions, since a large amount of the He^+ ions are neutralized during backscattering and the backscattered ion yield is already relatively low [6]. Contrast in backscattered ion images alone does not allow for the identification of different elements as a result of the oscillatory behavior of backscatter yield with atomic number Z, as explained in Section 4.2. Thus, it is necessary to measure the energy E_{BS} of backscattered particles: this depends on the primary beam energy, the angle of the incident ion beam, and the ratio of beam/target masses. Then, once E_{BS} is collected, if the other variables are known including the incident ion mass, the target particle mass is calculable [13]. This is merely an approximation, assuming that there is conservation of momentum in the scattering event. The expression describing the backscattering scenario is

$$E_{BS} = E_P \cdot \left(\frac{\sqrt{M_2^2 - M_1^2 \sin^2(\theta)} + M_1 \cos(\theta)}{M_1 + M_2} \right)^2 \tag{6}$$

where E_{BS} is the backscattered ion energy, E_P is the energy of the incident ion beam, M_1 is the mass of a helium ion, M_2 is the unknown mass of a target particle, and θ is the scatter angle [15]. This relationship is plotted for ratios of E_{BS}/E_P vs. target mass for a helium ion with backscatter angle 115° in Fig. 10a. This demonstrates how particles with low target masses will be easier to distinguish as a result of the high slope in the region between 0-75 amu. As a result, backscatter energies will largely vary for particles with low masses. Of course, this is just an approximation, but this should theoretically describe the phenomena.

Fig. 10b displays experimental spectra for various solid samples, demonstrating backscatter counts as a function of backscatter energy. A fixed-position solid state detector is used for this experiment with 4keV resolution [15]. The leftmost edge of the spectra represents deep scattering events causing higher energy loss and hence low backscattered energies: this gives insights into the sample composition deep into a sample. The highest energies on the spectra indicate scattering from the surface of the samples with minimal energy loss. This proof-of-concept demonstrates how backscatter energies and yields may be used to distinguish between elements by comparing

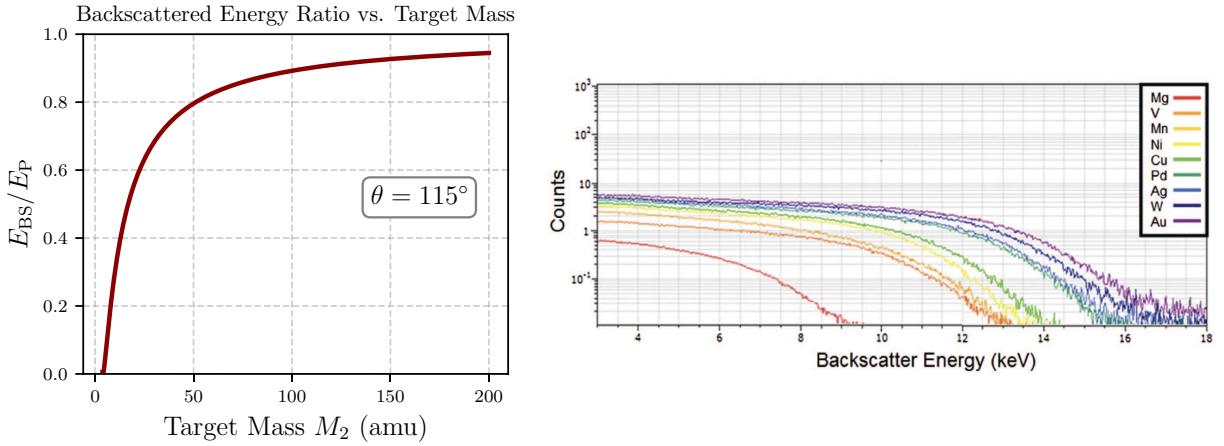


Figure 10: (a) Ratio of backscattered energy divided by incident ion energy, E_{BS}/E_P vs. target particle mass plotted for incident helium ions for a detector angle of 115° using Equation 6. (b) Experimental energy spectra of backscatter counts vs. backscatter energy for various pure elements using a solid state detector on the ORION HIM, reproduced from [15].

with simulations or known results. It is best suited for distinguishing between elements far apart: for consecutive elements, the experimental data shows that low-mass particles are more easily distinguished, for example Ni and Cu vs. Pd and Ag. However, this method is still quite limited and time consuming.

6 Comparison to Scanning Electron Microscopy (SEM)

While HIM and SEM are very similar techniques, helium ion microscopy poses several advantages for imaging samples compared to scanning electron microscopy. The main advantages are the improved depth of field and decreased interaction volume (and hence improved edge clarity) as a result of the unique helium ion beam properties and the helium ion's small wavelength.

Fig. 11 presents SEM and HIM images at various fields of view (FOV) for a dried *Arabidopsis thaliana* structure. This is a plant sample that has no coating or sample preparation besides drying [12]. Since the sample is uncoated, the SEM images were taken at <1kV to minimize charging artifacts and in an attempt to attain the best surface resolution by minimizing interaction volume. Still, at FOVs of 3.4µm and below, charging effects are seen with streaks, bands, or apparent motion

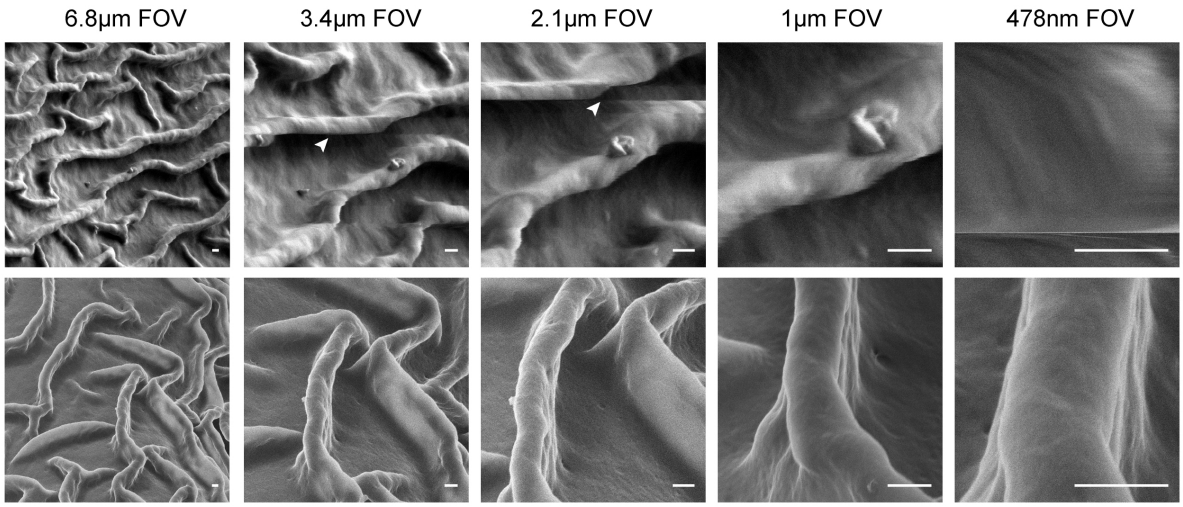


Figure 11: High magnification series of uncoated and critical point dried *Arabidopsis thaliana* sepal cuticle structures, imaged with a SEM and HIM. The top row presents the sample imaged with a <1kV electron beam with an ET detector. Small white pointers point to charging artifacts in the images. The bottom row presents the sample imaged with a helium ion beam. Scale bars are all 200nm. Figure reproduced from [12].

in the images. In contrast, no charging effects are present in the HIM images as a result of the effective electron flood gun. In general, the HIM images have uniform gray levels as a result of the high depth of field and high SE yield, while the SEM images depict dark shadows in the troughs of the sample. At all FOVs, the HIM images have very well defined edge clarity and surface definition. At 2.1µm and below, the SEM images are too blurry and do not capture the edges of the structure very well. At the smallest FOV, charging, thermal drift, and beam damage render the SEM image unusable, while the HIM image is still very clear [12].

Fig. 12 presents another comparison between a sample imaged with HIM and SEM techniques. The grey levels in the HIM image in Fig. 12a are much more uniform and consistent, compared to the SEM image in Fig. 12b which has a much greater range of gray levels which are especially noticeable in the background and on the rightmost nanowire. The uniformity of the HIM image results from the improved depth of field and consistent SE yield. Additionally, the edge clarity is significantly better for the HIM image compared with the SEM image. Whereas the edges in the HIM image are sharp, the entire SEM image appears as blurred which makes it difficult to discern where the actual edges of the nanowires are. This primarily results from the different interaction

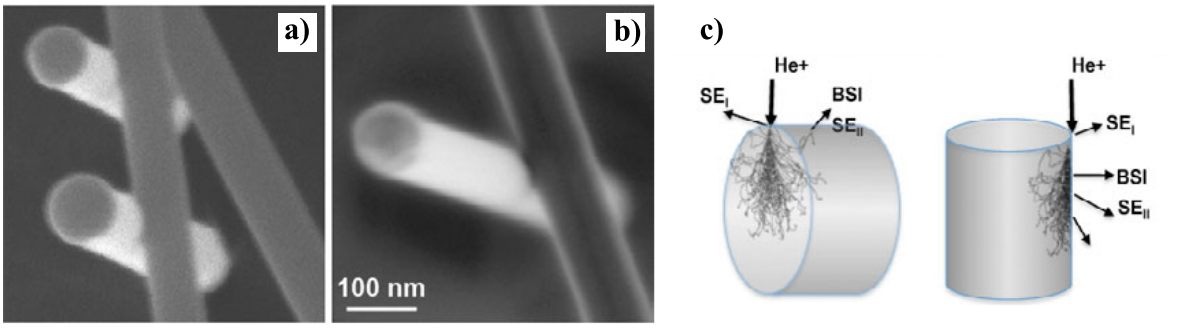


Figure 12: Comparison of HIM and SEM images of an InAs nanowire and the corresponding interaction volume yielding the image contrast. (a) HIM image taken at 20kV with an ET detector. (b) SEM image at 0.5kV taken with an in in-lens SE detector. (c) Comparison of helium ion interaction volumes in perpendicular and parallel oriented nanowires. Figure adapted from [14]

.

volumes of the two beam types and the fact that SEs from the HIM are much more localized to the probe area. These images also provide a great example of image contrast as a result of the beam interaction volume and sample geometry. The following discussion applies to either the SEM or HIM image. Despite the nanowires being the same material, one appears as very bright around its diameter while the other appears as a dark gray. When the nanowires are arranged perpendicularly to the ion beam, as in the first scenario in Fig. 12c, the interaction volume of the ion beam is primarily in the bulk of the nanowire and hence secondary electrons only escape from a small region at the surface of the wire. This results in the consistent gray levels around the diameter of the nanowires. Conversely, nanowires parallel to the ion beam have edges that appear bright and faces that appear as a darker gray. The bright edges result since SEs may easily escape from the sides of the cylindrical wire when the beam is incident near the edges. This also explains why the edges of the perpendicular nanowires have a slight halo effect in Fig. 12a.

Unfortunately, HIM does not allow for x-ray spectroscopy analysis as with SEMs to determine elemental information. For reference, x-rays are emitted when a particle excites an inner-shell electron: as the hole is filled by a valence electron, an x-ray may be emitted with the energy difference. Each element will have specific characteristic x-ray emission. Helium ion beams at 30keV produce negligible x-ray signals as a result of the low ion velocities [13]. A study found that a 12.5 hour exposure of a copper sample to a 29.5 keV helium ion beam with a high current

of 375 pA only yielded a Cu peak with just *50 counts* [13]. From this experimental data, the x-ray yield can be inferred as less than 10^{-10} per ion: this is almost 7 orders of magnitude lower than an electron beam with comparable energy. Thus, the relatively low energy helium ion beams are massively inefficient at ejecting core shell electrons, and x-ray analysis is simply infeasible with HIMs. Still, the SIMS technique combined with HIM is an extremely powerful methodology for determining surface composition of a sample, perhaps more powerful than Energy Dispersive X-ray Spectrometry (EDXS) with SEMs.

7 Applications of HIM

HIM has various applications across nanotechnology, materials science, and biology. The technique is extremely versatile, allowing for high-resolution nanoscale analysis of samples. The breadth of signals emitted from a sample irradiated by an ion beam allows for deep analysis and understanding of samples beyond the topographical information depicted in SE images. The following sections give an overview of different techniques that may be performed with a helium ion microscope.

7.1 High-Resolution Imaging of Biological Samples

HIM is a valuable technique for the surface imaging of biological samples: it offers high depth of field and high resolution, requiring minimal sample preparation. The high resolution and low interaction volume of helium ions is crucial for revealing subtle details about the structure of a surface. Furthermore, HIM is extremely attractive for biological samples in particular since surfaces may remain uncoated and non-conductive due to the electron flood gun.

Fig. 13 presents a series of HIM images of a single scale taken from a butterfly wing. The HIM is able to beautifully image the sample with extreme detail and clarity. As a result of the high depth of field, Fig. 13c even images within the cell-like network of the scale, revealing some information deep below the surface. While this area is slightly shadowed due to the structure, it is still in focus. The structure depicted is responsible for scattering incident light within, having high absorption

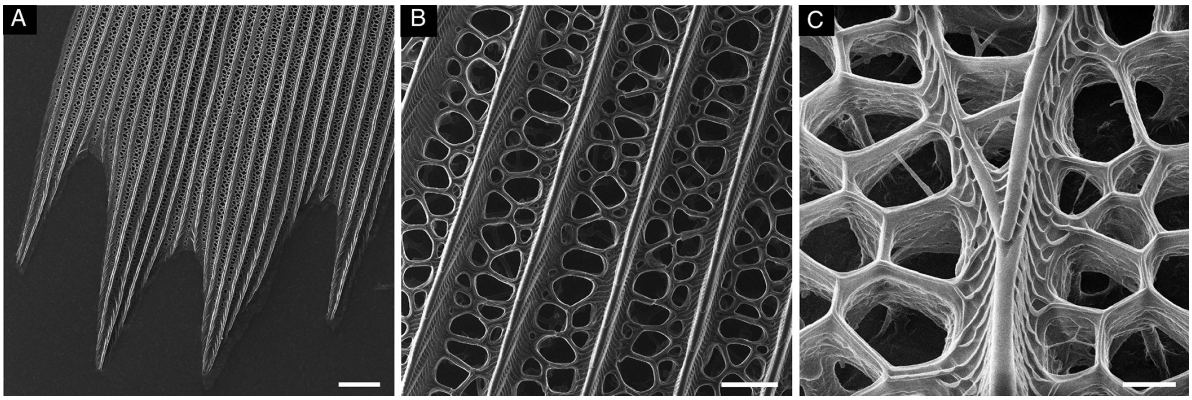


Figure 13: HIM images of a Blue Mountain Butterfly scale at various magnifications taken at 30kV. (a) 10µm scale bar, 0° tilt; (b) 2µm scale bar, 0° tilt; (c) 400nm scale bar, 21° tilt. Adapted from [16].

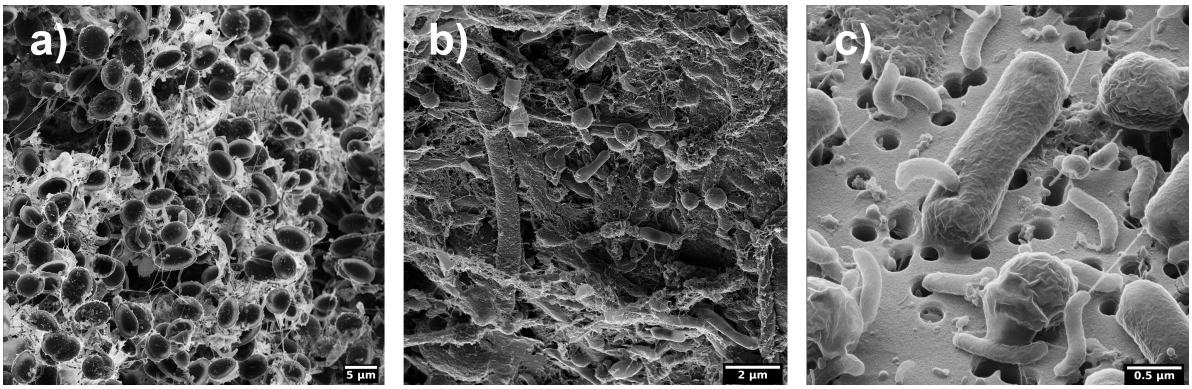


Figure 14: Assortment of HIM images for biological applications. (a) A biofilm of *Chlorella* microalgae. (b) Microbial mat collected at the Himalayan hot springs at Manikaran imaged with the HIM. (c) Predatory bacterium *Bdellovibrio bacteriovorus* infecting *Escherichia coli*. Images adapted from [17].

resulting in the scales having a black appearance [16]. Overall, this is a beautiful set of images that very clearly depicts the structure of the scale from a butterfly wing. There are no charging artifacts, blurry regions, or abnormalities in these images.

Fig. 14 presents an assortment of HIM images taken for other biological applications. Despite the almost 20µm topographical variation within the FOV in Fig. 14a, almost the entire sample remains in crisp focus as a result of the high HIM depth of field. The remaining images depict the incredible detail and clarity that is achieved with the HIM with these uncoated, non-conductive samples. HIM imaging produces extremely visually striking images with exceptional clarity and detail, directly as a result of the optimal helium ion beam properties and sample interaction.

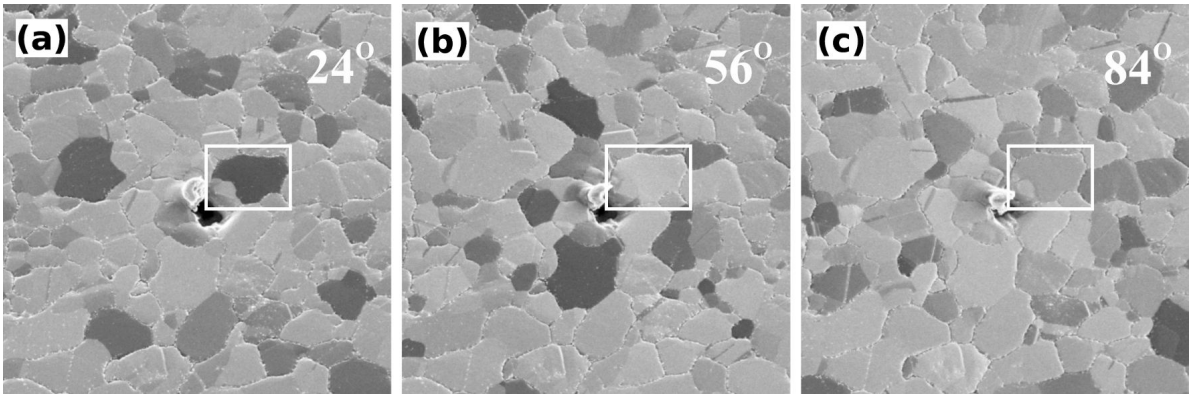


Figure 15: Secondary electron images of an annealed polycrystalline Au film with a 15kV helium ion beam. The film has a 111 texture. Each panel presents the sample at various tilt angles. The rectangular box encloses the same grain in all three panels, for alignment purposes. Reproduced from [18].

7.2 Crystallographic Orientation Mapping

Due to ion channeling contrast in secondary electron or backscattered ion images, crystallographic orientations of grains in polycrystalline samples may be mapped. This technique may be performed more easily using SEs since they have much higher yield than backscattered ions. Fig. 15 presents this technique. Note that the beam energy is lower than the typical 30keV, in order to increase ion channeling contrast [18]. Fig. 15a depicts how the grain boundaries are easily visible and grains have varying gray levels as a result of differing degrees of ion channeling. When the sample is tilted to other angles, the ion channeling contrast changes. The grain that was a dark gray in Fig. 15a transforms to much lighter tones when the sample tilt angle is increased. With SE images, it is acceptable to repeatedly image the sample at different angles: the SE escape depth is only several nanometers, and any ion-induced defects will be much deeper into the sample. These defects will impact the backscattered ion images but not significantly impact the SE images, with a 1% estimated defect density at 3nm after recording 30 SE images [18]. A map of low-index directions resulting in ion channeling may then be simulated using the known FCC structure of gold. Then, finally, the grains in the SE images at various tilt angles may be mapped to certain grain orientations. This is a complex process, but the resulting grain orientation map is shown in Fig. 16. Most grains are definitively mapped to specific orientations, although some have a small degree of uncertainty

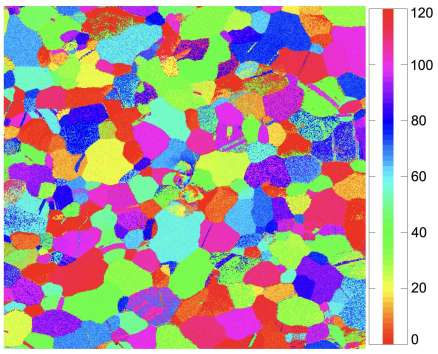


Figure 16: Color-coded orientation map of a polycrystalline gold film. The colors indicate the azimuthal angle from the [111] surface normal for a 35° sample tilt, reproduced from [18].

where there are two plausible orientations (colors) mapped to the same grain.

7.3 Subsurface Imaging

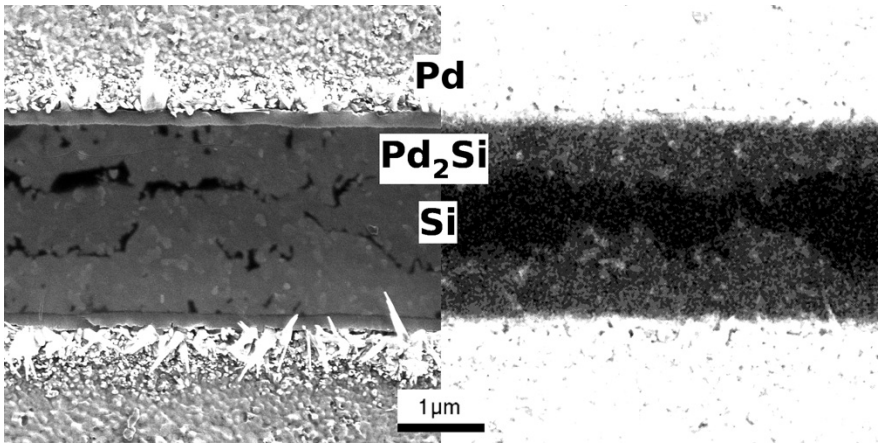


Figure 17: Split-view simultaneous image of Pd_2Si interconnects covered with SiO_2. The left half of the image is the SE image and the right half is the back-scattered ion image. Reproduced from [8].

Rutherford backscatter imaging may reveal information below films of low atomic number materials as a result of their low backscatter yields. This is especially powerful for visualizing diffusional processes without disturbing a sample. This technique is presented in Fig. 17, capturing both SE and backscatter images simultaneously. In the SE image on the left, there is great surface detail of the Pd interconnects at the top and bottom of the image. Between these regions is what appears to be a uniform oxide layer of SiO_2 with some slight cracks. These cracks have been formed

after an annealing process where the Pd has diffused through the underlying Si layer [7]. Switching to the back-scattered image, there is new information revealed. The top and bottom bright regions still are the Pd interconnects which have high backscatter yields. Now, however, the central region directly depicts the Si substrate (dark, center) and adjacent above and below are diffused regions of Pd_2Si, diffused from the upper and lower Pd contacts. This diffusion is non-uniform across the length of the sample and is not at all clear from the SE image due to the cracking of the SiO_2 film. This information is critical in the fabrication of devices and would not otherwise be available using cross-sectional techniques like FIB [8]. This demonstrates the ability to visualize diffusion under thin films using backscatter imaging with HIM.

7.4 Ionoluminescence Imaging

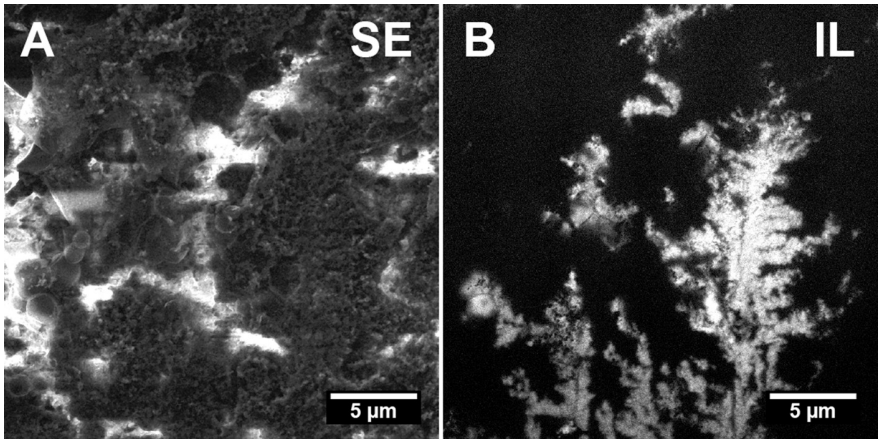


Figure 18: Simultaneously captured secondary electron (a) and ionoluminescence (b) images of an NaCl residue on an aluminum substrate. The FOV is 25µm and the acceleration voltage is 35kV. Reproduced from [8].

Although ionoluminescence is a relatively experimental technique, there are several studies that explore its use with various types of materials. Fig. 18 explores ionoluminescence of NaCl residue (an alkali halide) on an aluminum substrate. In the SE image in Fig. 18a, the bright areas are the aluminum substrate while the darker areas are the NaCl residue. This is an example of material contrast, where the aluminum clearly has higher secondary electron yield. In the IL image in Fig. 18b, the contrast is effectively swapped: the bright regions are due to the ionoluminescence

of the NaCl, while the dark regions are the aluminum substrate. The incident ion beam enhances IL as a result of defect production by the ion beam in alkali halides. This is intrinsic IL, resulting from recombination of electrons in the sample [8]. Thus, this demonstrates the feasibility of IL imaging with HIM, with the ability to capture both SE and IL images simultaneously.

7.5 SIMS Imaging

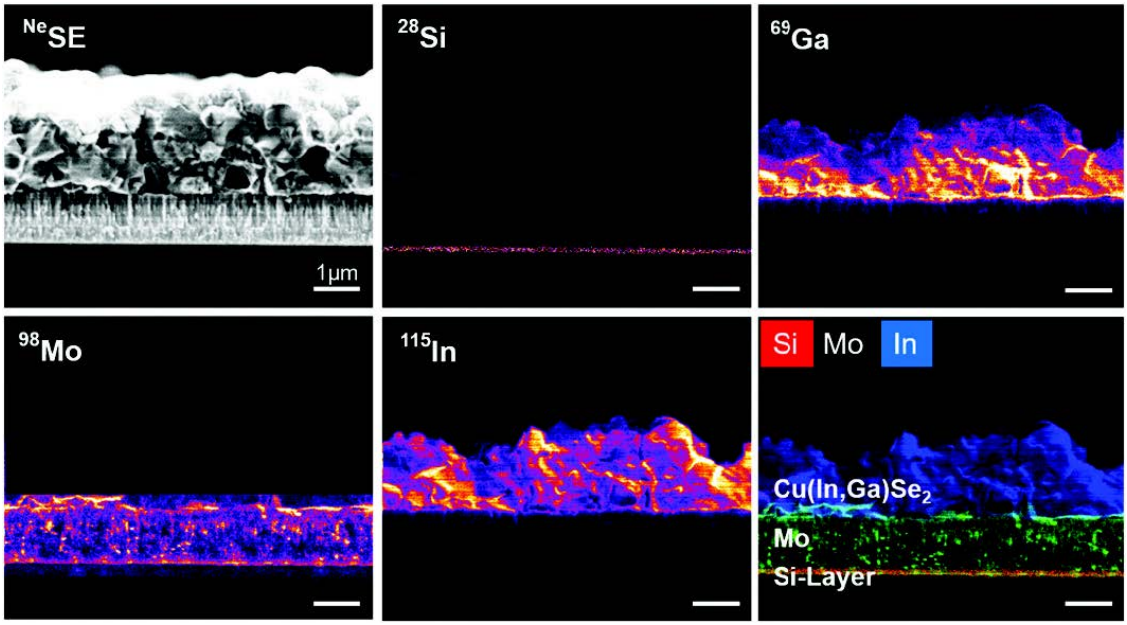


Figure 19: HIM-SIMS analysis of the cross section of a CIGS thin film device. Both SE and SIMS images were acquired with a 25kV Ne^+ beam. Silicon, gallium, molybdenum and indium were detected simultaneously at a resolution of 512×512 pixels with a dwell time of 2ms per pixel. Scale bar: 1µm. Reproduced from [13].

Imaging utilizing the SIMS technique allows for the creation of information-rich and visually striking images depicting the elemental composition of nanoscale surfaces. Copper indium gallium selenide (CIGS) thin films have been used to produce high yield photovoltaic cells. The SIMS technique allows for the analysis of the constituent elements and to analyze diffusion or trace elements within fabricated devices [13]. Fig. 19 displays a series of HIM and SIMS images of the cross-section of a mechanically-cleaved CIGS device. From bottom to top, the layers of the device are: glass substrate, Si layer, Mo layer, and finally, the sunlight absorption layer of

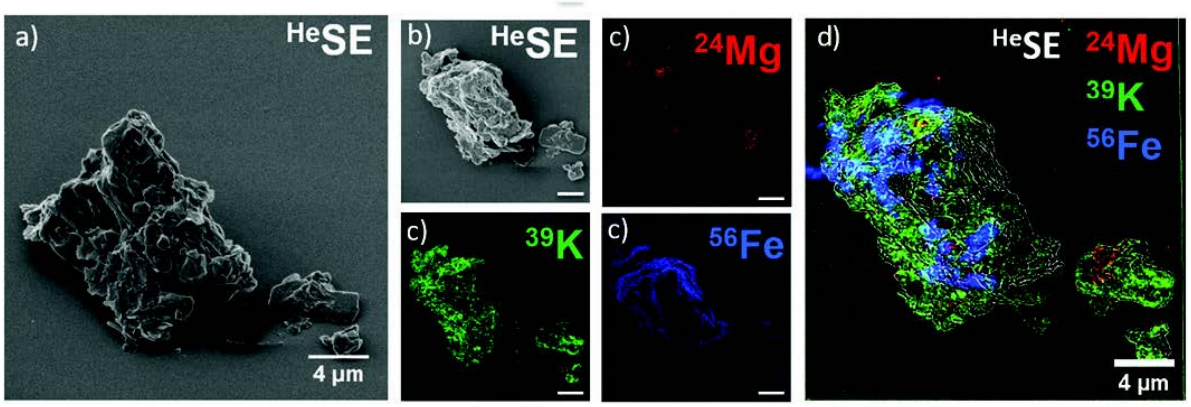


Figure 20: HIM-SIMS imaging analysis for a soil micro-aggregate. (a) SE image obtained with a 25kV He^+ beam and 45° stage tilt. (b) SE image obtained with a 25kV He^+ beam and no stage tilt. (c) SIMS images (^{24}Mg, ^{39}K, ^{56}Fe) acquired with a 20kV Ne^+ beam in a matrix of 512×512 pixels and a dwell time of 3 ms per pixel. (d) The SE and SIMS overlay image fused by Laplace image fusion. Scale bars: 4µm. Reproduced from [13].

Cu(In, Ga)Se_2. Although the SE image produced with the neon ion beam has lower resolution than images taken with a helium ion beam, the neon beam is better-suited for SIMS and allows for quicker data-collection without requiring the gas in the GFIS to be swapped. In the subsequent images, the brighter (more yellow/white) pixel intensities correspond to higher concentrations of the given element. This demonstrates that silicon is only present as a thin layer atop the glass substrate. The molybdenum atop the silicon actually has somewhat diffused into the silicon, indicated by the sparse light blue spots beneath the bright yellow line at the interface between the layers. Indium and gallium have relatively similar intensity distributions in their constituent SIMS images. For both, the atoms have clearly diffused to the Mo layer, as indicated by sporadic "roots" traveling vertically downwards. Finally, the combined color-coded image depicts the regions of different constituents, including the presence of diffusion. SIMS allows for this information-rich compositional analysis that otherwise would not be possible with the grayscale SE image.

Another application of the HIM-SIMS imaging technique is presented in Fig. 20 for the compositional analysis of a soil particle. This time, the composition of the soil particle is unknown ahead of time. High resolution images are obtained to view the topography of the sample using a helium ion beam. Then, SIMS images are obtained with a neon ion beam in order to

determine the constituent elements of the soil particle, pinpointing the exact isotopes present with the mass spectrometer. The SE image is then fused with the SIMS images for potassium, iron, and magnesium through a Laplace fusion process. This yields Fig. 20d which demonstrates the exact spatial composition and texture of the particle. The soil micro-aggregate is primarily composed of potassium with iron interspersed through its central region. There are also trace amounts of magnesium dispersed in various regions of the particle. Thus, SIMS imaging allows for extremely detailed elemental analysis of sample surfaces, with the potential to create information-dense and extremely striking images with a high level of detail.

8 Summary and Future Perspectives

The commercial future of helium ion microscopy is currently uncertain with no active vendors. Nonetheless, HIMs are tremendously powerful tools for nanoscale characterization and analysis, especially for biological study. With exceptionally high-resolution surface imaging, precise ability for elemental analysis with SIMS, and the capability to perform subsurface imaging and crystallographic mapping with backscattered ions, HIM surpasses the limitations of traditional SEMs in many aspects. Future developments will likely refine these existing techniques, enhancing HIM's current capabilities. The technique is especially well-suited for analyzing increasingly-small nanostructures, advanced materials, and biological systems. Even if HIMs remain a specialized tool, they will continue to have a crucial role for ultra-high-resolution imaging and analysis at the forefront of cutting-edge research.

References

ZEISS ORION NanoFab: Three Ion Beams for Enhanced Flexibility in Sub-10 nm Fabrication (tech. rep.). (2016). Carl Zeiss Microscopy GmbH. Jena, Germany.

Joy, D. C. (2013). *Helium Ion Microscopy: Principles and Applications*. Springer. https://doi.org/10.1007/978-1-4614-8660-2

Notte, J., Ward, B., Economou, N., Hill, R., Percival, R., Farkas, L., & McVey, S. (2007). An Introduction to the Helium Ion Microscope. *AIP Conference Proceedings*, *931*(1), 489–496. https://doi.org/10.1063/1.2799423

Escovitz, W. H., Fox, T. R., & Levi-Setti, R. (1975). Scanning transmission ion microscope with a field ion source. [Publisher: Proceedings of the National Academy of Sciences]. *Proceedings of the National Academy of Sciences*, *72*(5), 1826–1828. https://doi.org/10.1073/pnas.72.5.1826

Hlawacek, G., & Gölzhäuser, A. (Eds.). (2016). *Helium Ion Microscopy*. Springer International Publishing. https://doi.org/10.1007/978-3-319-41990-9

Audinot, J.-N., Philipp, P., De Castro, O., Biesemeier, A., Hoang, Q. H., & Wirtz, T. (2021). Highest resolution chemical imaging based on secondary ion mass spectrometry performed on the helium ion microscope [Publisher: IOP Publishing]. *Reports on Progress in Physics*, *84*(10), 105901. https://doi.org/10.1088/1361-6633/ac1e32

Gastel, R. v., Hlawacek, G., Zandvliet, H. J. W., & Poelsema, B. (2012). Subsurface analysis of semiconductor structures with helium ion microscopy. *Microelectron. Reliab.*, *52*(9-10), 2104–2109. https://doi.org/10.1016/J.MICROREL.2012.06.130

Hlawacek, G., Veligura, V., van Gastel, R., & Poelsema, B. (2014). Helium ion microscopy. *Journal of Vacuum Science & Technology B*, *32*(2), 020801. https://doi.org/10.1116/1.4863676

Kanaya, K., & Okayama, S. (1972). Penetration and energy-loss theory of electrons in solid targets. *Journal of Physics D: Applied Physics*, *5*(1), 43. https://doi.org/10.1088/0022-3727/5/1/308

Seiler, H. (1983). Secondary electron emission in the scanning electron microscope. *Journal of Applied Physics*, *54*(11), R1–R18. https://doi.org/10.1063/1.332840

Shih, A., Yater, J., Hor, C., & Abrams, R. (1997). Secondary electron emission studies. *Applied Surface Science*, *111*, 251–258. https://doi.org/10.1016/S0169-4332(96)00729-5

Joens, M. S., Huynh, C., Kasuboski, J. M., Ferranti, D., Sigal, Y. J., Zeitvogel, F., Obst, M., Burkhardt, C. J., Curran, K. P., Chalasani, S. H., Stern, L. A., Goetze, B., & Fitzpatrick, J. A. J. (2013). Helium Ion Microscopy (HIM) for the imaging of biological samples at sub-nanometer resolution [Publisher: Nature Publishing Group]. *Scientific Reports*, *3*(1), 3514. https://doi.org/10.1038/srep03514

Wirtz, T., De Castro, O., Audinot, J.-N., & Philipp, P. (2019). Imaging and Analytics on the Helium Ion Microscope. *Annual Review of Analytical Chemistry*, *12*(1), 523–543. https://doi.org/10.1146/annurev-anchem-061318-115457

Bell, D. C. (2009). Contrast Mechanisms and Image Formation in Helium Ion Microscopy. *Microscopy and Microanalysis*, *15*(2), 147–153. https://doi.org/10.1017/S1431927609090138

Sijbrandij, S., Thompson, B., Notte, J., Ward, B. W., & Economou, N. P. (2008). Elemental analysis with the helium ion microscope. *Journal of Vacuum Science & Technology B: Microelectronics and Nanometer Structures Processing, Measurement, and Phenomena*, *26*(6), 2103–2106. https://doi.org/10.1116/1.2993262

Boden, S. A., Asadollahbaik, A., Rutt, H. N., & Bagnall, D. M. (2012). Helium ion microscopy of Lepidoptera scales [_eprint: https://onlinelibrary.wiley.com/doi/pdf/10.1002/sca.20267]. *Scanning*, *34*(2), 107–120. https://doi.org/10.1002/sca.20267

Schmidt, M., Byrne, J. M., & Maasilta, I. J. (2021). Bio-imaging with the helium-ion microscope: A review. *Beilstein Journal of Nanotechnology*, *12*, 1–23. https://doi.org/10.3762/bjnano.12.1

Veligura, V., Hlawacek, G., Gastel, R. v., Zandvliet, H. J. W., & Poelsema, B. (2012). Channeling in helium ion microscopy: Mapping of crystal orientation [Publisher: Beilstein-Institut]. *Beilstein Journal of Nanotechnology*, *3*(1), 501–506. https://doi.org/10.3762/bjnano.3.57